RSC Advances

PAPER

View Article Online
View Journal | View Issue

Cite this: *RSC Adv.*, 2021, **11**, 1022

N-doped mixed Co, Ni-oxides with petal structure as effective catalysts for hydrogen and oxygen evolution by water splitting†

Hai Zhong,‡[a] Guofeng Cheng,‡[b] Guangcai Ma,[b] Enhui Wu,[c] Zhuo Zhang,[b] Xuefeng She,*[a] Shuqiang Jiao,[a] Jingsong Wang[a] and Qingguo Xue[a]

Developing electrocatalytic nanomaterials for green H_2 energy is inseparable from the exploration of novel materials and internal mechanisms for catalytic enhancement. In this work, nano-petal N-doped bi-metal (Ni, Co) and bi-valence (+2, +3) $(Ni_{1-x}Co_x)^{2+}Co_2^{3+}O_4$ compounds have been *in situ* grown on the surface of Ni foam. The N^{3-} atoms originate from the amino group in urea and doped in the compound during annealing. The as-synthesized N-doped $(Ni_{1-x}Co_x)^{2+}Co_2^{3+}O_4$ nano-petals demonstrate commendable hydrogen evolution reaction (HER) and oxygen evolution reaction (OER) bi-functional catalytic efficiency and stability. Electrochemical measurements confirm that the nitrogen doping significantly improves the catalytic kinetics and the surface area. Density functional theory calculations reveal that the improved HER and OER kinetics is not only due to the synergistic effect of bi-metal and bi-valence, as well as the introduction of defects such as oxygen vacancies, but also it more depends on the shortened bond length between the nitrogen N^{3-} atoms and the metal atoms, and the increased electron density of the metal atoms attached to the N^{3-} atoms. In other words, the change of lattice parameters caused by nitrogen doping is more conducive to the catalytic enhancement than the synergistic effect brought by bi-metal. This study provides an experimental and theoretical reference for the design of bi-functional electrocatalytic nanomaterials.

Received 17th October 2020
Accepted 30th November 2020

DOI: 10.1039/d0ra08846c

rsc.li/rsc-advances

1. Introduction

In response to the energy and environmental crisis, many countries are devoted to developing practical electrocatalytic materials for hydrogen and oxygen evolution by water splitting. As benchmarks, Pt is considered to be the most efficient catalyst for hydrogen evolution reaction (HER),[1,2] while RuO_2 and IrO_2 have the leading positions for oxygen evolution reaction (OER).[3,4] However, their rarity and high price greatly limit their industrialization and commercialization. Therefore, highly active and cost-effective catalysts are in urgent need to replace the precious metal catalysts. Recently, transition metal nickel (Ni) and cobalt (Co), and their compounds, such as (hydro)oxides, nitrides, and carbides, have attracted tremendous attention due to their intrinsic catalytic activity, environmental-friendliness and earth-abundance.[5–10] Through intracrystalline or surface modification, Ni (or Co)-based catalysts can obtain comparable HER or OER performance with noble metal catalysts.

For commercializing the catalysts, low-cost and bi-functionality in both HER and OER have long been the primary targets. Compared with the single-transition-metal-based catalysts, the bimetallic Ni–Co-based catalysts are more active to overcome the sluggish kinetics of OER with four electrons transfer, and thus possess commendable overpotentials for both HER and OER.[11] For example, $NiCo_2O_4$/CoO/graphite composite can act as remarkable OER catalysis with an overpotential of 323 mV (*vs.* RHE) (recorded at 10 mA cm^{-2}), which is superior to that of IrO_2 (340 mV) and RuO_2 (350 mV).[12] Researchers attributed the highly improved electrocatalytic activity to the electron hopping between different valence states of Ni and Co, and also the redox couples of Co^{3+}/Co^{2+} and Ni^{3+}/Ni^{2+}.[13] As for alloys, Fu *et al.* revealed that Ni–Co alloy nanoparticles could even rival commercial Pt/C and RuO_2 catalysts owing to the "rich valence state changes" between Ni and Co.[14] Moreover, a large number of density functional theory studies have shown that the mixture of bi-metal and bi-valence can effectively increase the number of defects such as oxygen vacancy, thereby increasing the number of active sites as well as the density of electron cloud around them and consequently

[a]State Key Laboratory of Advanced Metallurgy, University of Science and Technology, Beijing, 100083, China. E-mail: shexuefeng@ustb.edu.cn
[b]School of Physics and Physical Engineering, Qufu Normal University, Qufu, 273165, China
[c]Panzhihua International Research Institute of Vanadium and Titanium, Panzhihua University, Panzhihua, 617000, China

† Electronic supplementary information (ESI) available. See DOI: 10.1039/d0ra08846c

‡ Co-author.

greatly reducing the free energy for both adsorption and desorption of intermediates.[15]

Beside bi-metallic oxides, in recent years, bi-metallic nitrides such as $NiCo_2N$, NiMoN, $FeNi_3N$, *etc.* have also attracted increasing attention due to their enhanced activity for water oxidation and reduction.[16–18] Peng has proven that transition metal nitride has excellent electrocatalytic activity, stability and corrosion resistance, and it is a good substitute for noble metals in water splitting system.[19] Yu Zhang *et al.* also demonstrated that the electronic structure of this metal nitride can be appropriately adjusted to promote the rapid transfer of electrons due to the inclusion of interstitial nitrogen atoms, thus greatly reducing the energy barrier to improve its catalytic activity.[20] Considering the significant improvement of HER and OER kinetics *via* bimetallic and bivalent mixing, as well as nitrogen doping as mentioned above, it is very essential to combine the above three advantages in a bifunctional nano-catalytic system. Furthermore, it is of great significance to evaluate whether bimetal or nitrogen doping plays a much stronger role in improving catalytic efficiency.

In this work, large-scale and vertically aligned N-doped $(Ni_{1-x}Co_x)^{2+}Co_2{}^{3+}O_4$ nano-petals have been fabricated on the surface of Ni foam. The unique morphology like rose petals (Fig. 1a) enables the spacing between nano-petals to facilitate the chemical reactions and the evolution of hydrogen and oxygen. Electrochemical experimental results show that Ni–Co bimetal and bivalence (+2, +3), as well as nitrogen doping, can greatly improve HER and OER efficiencies; theoretical studies *via* density functional calculation reveal that these efficiencies improvement are due to the slight changes in atomic spacing, which greatly increases the number of defects and the electron densities. The effect of bimetal and nitrogen doping on catalytic performance enhancement has also been compared. The excellent HER and OER performances endowed by N-doped $(Ni_{1-x}Co_x)^{2+}Co_2{}^{3+}O_4$ nano-petals provide a technical and theoretical reference for the future design of bi-functional electrocatalytic materials.

2. Experimental and calculation section

2.1. Materials

Nickel nitrate hexahydrate $[Ni(NO_3)_2\cdot 6H_2O]$, cobalt nitrate hexahydrate $[Co(NO_3)_2\cdot 6H_2O]$, urea (CH_4N_2O), hexadecyl trimethyl ammonium bromide (CTAB, $C_{19}H_{42}BrN$), potassium hydroxide (KOH) were purchased from Aladdin. Ni foam was provided by JD.com. Prior to use, the Ni foam was cleaned by sonicating successively with acetone, ethanol and DI water for 10 min each.

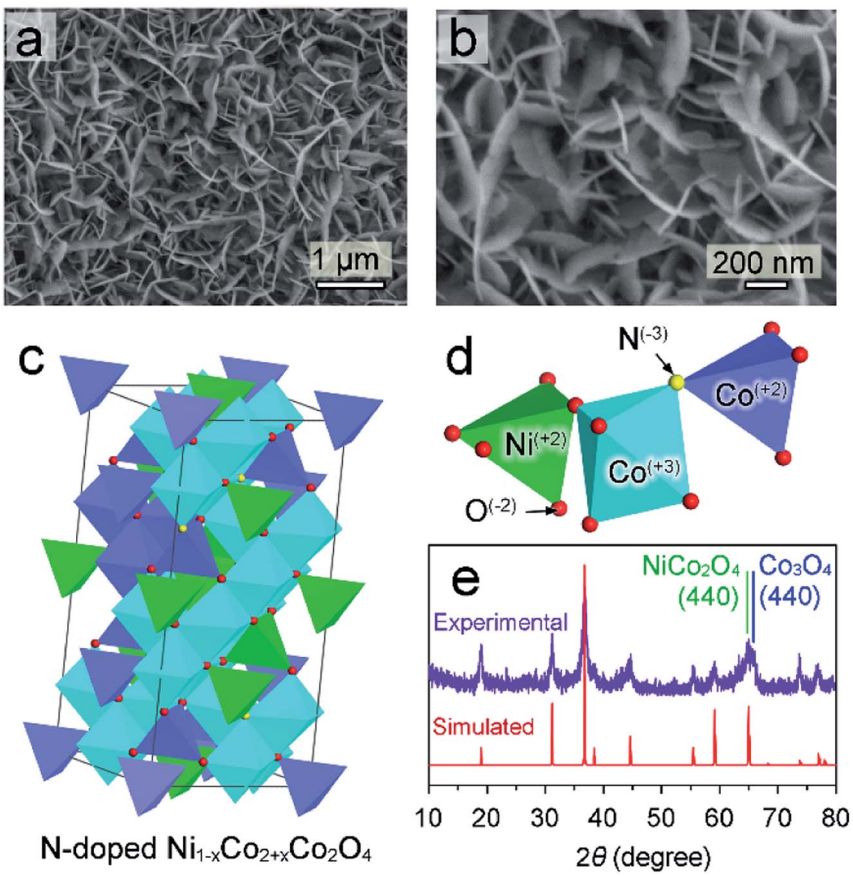

Fig. 1 (a and b) Top-view SEM images of N–$Ni_{1-x}Co_{2+x}O_4$ NPs; (c and d) crystal structure (c) and legend (d) of N-doped $Ni_{1-x}Co_{2+x}O_4$; (e) experimental (upper row) and simulated (bottom row) XRD patterns of the N–$Ni_{1-x}Co_{2+x}O_4$ NPs.

2.2. Preparation of N-doped $(Ni_{1-x}Co_x)^{2+}Co_2^{3+}O_4$ nanopetals

At first, 1 mmol $Ni(NO_3)_2 \cdot 6H_2O$ and 3 mmol $Co(NO_3)_2 \cdot 6H_2O$ were dissolved in 50 mL DI water, and 2 mmol urea and 1 mmol CTAB were dissolved in another 50 mL DI water by sufficient stir. Then, the above two solutions were mixed together. Next, pieces of Ni foam with 1 cm × 2 cm size were dipped into the glass bottle containing the mixed solution. After that, the bottle was put into air dry oven at 95 °C for 15 h. After 15 hours, the Ni foam was taken out from the bottle, followed by cleaning and drying. Finally, the Ni foam was placed in a tubular furnace and annealed at 300 °C in nitrogen atmosphere for 1 h.

2.3. Characterization

SEM measurement was carried out on a XL 30S FEG scanning electron microscope at an acceleration voltage of 20 kV. XRD patterns were acquired using a D/MAX-2500/PC X-ray diffractometer equipped with a Cu Kα radiation source. The structures of the samples were characterized by a JEM-2200FS transmission electron microscopy (TEM) operated at 200 kV. XPS measurement was performed using a VG ESCALAB 250 X-ray photoelectron spectrometer with Mg as the excitation source.

2.4. Electrochemical measurements

All of the electrochemical measurements were carried out using a CHI660E electrochemical workstation in a three electrodes system. As-grown samples, Pt wafer and saturated calomel electrode were used as the working, counter and reference electrodes, respectively. The *iR* correction was applied to all data. The experimental potentials were converted to RHE with the equation $E_{(RHE)} = E_{(calomel)} + (0.219 + 0.0591 \times pH)V$.[21] LSV measurements were performed in H_2-saturated 1.0 M KOH solution at a scan rate of 5 mV s^{-1}.

2.5. Density functional theory calculation

All of the density functional theory (DFT) calculations were performed using the CASTEP program available in Materials Studio. The plane wave basis set cutoff energy was 400 eV for geometry optimization and energy calculation. The generalized gradient approximation (GGA) with the Perdew–Burke–Ernzerhof (PBE) function was employed to present exchange–correlation interactions. The energy convergence tolerance for the self-consistent field (SCF) was 2.0×10^{-6} eV per atom. All

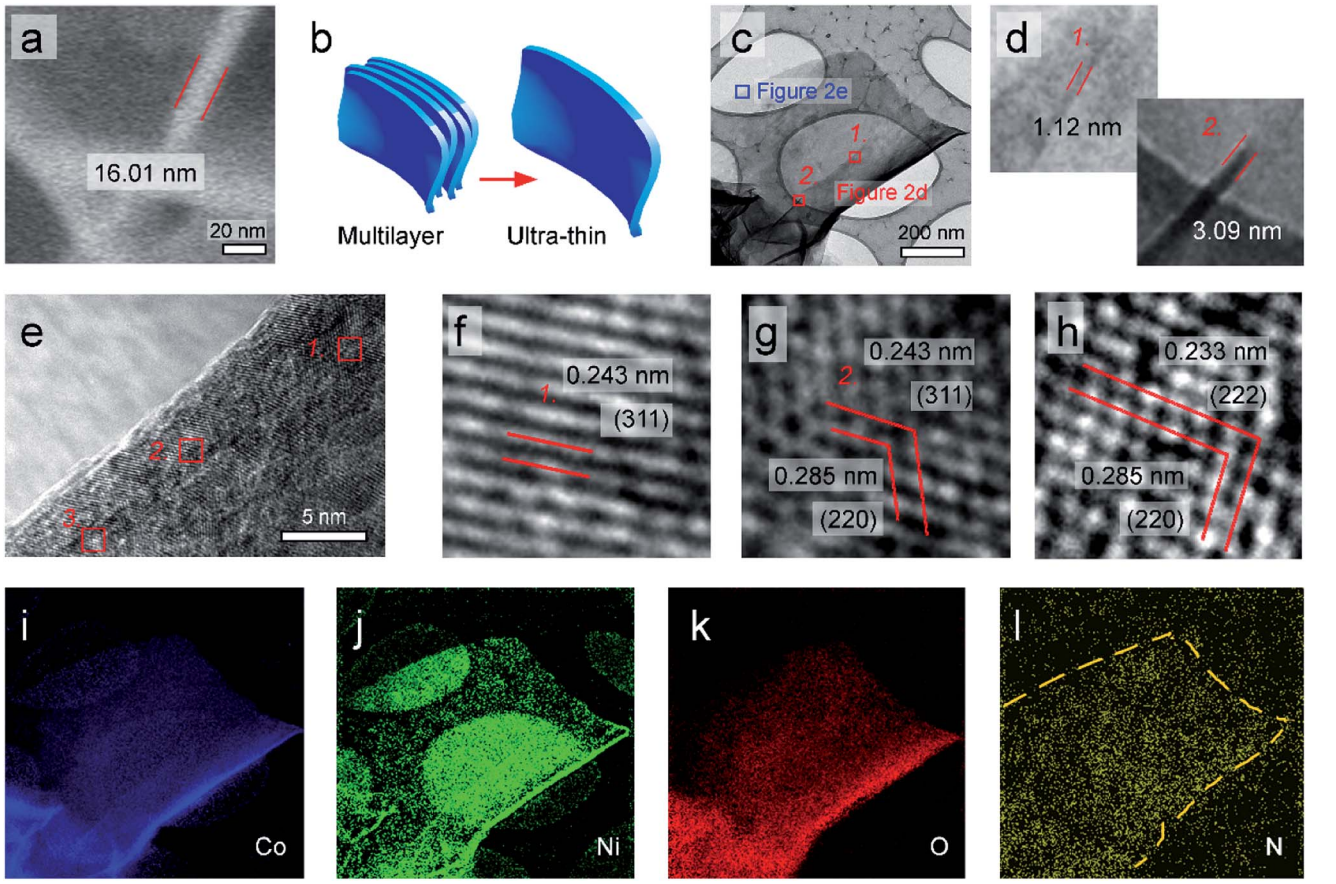

Fig. 2 (a) Close-up view of the N–$Ni_{1-x}Co_{2+x}O_4$ NPs; (b) schematic diagram of an individual petal with multilayer structure; (c) TEM image of the N–$Ni_{1-x}Co_{2+x}O_4$ NP; (d and e) enlarged views taken from the red (d) and blue (e) squares in (c); (f–h) HRTEM images taken from (e); (i–l) element mappings of Co(I), Ni (j), O (k) and N (l).

of the DFT calculations were carried out without spin restricted.

3. Results and discussion

3.1. Characterization of Ni, Co-samples

N-doped $(Ni_{1-x}Co_x)^{2+}Co_2{}^{3+}O_4$ nano-petals is abbreviated as N–$Ni_{1-x}Co_{2+x}O_4$ NPs in this work. The scanning electron microscope (SEM) image in Fig. 1a shows that large area N–$Ni_{1-x}Co_{2+x}O_4$ NPs with uniform thickness and a certain radian are evenly distributed on the surface of Ni foam. Fig. 1b displays that the arc-shaped nano-petals could support and leave space for each other, which prevents the nano-petals from collapsing and utilizes the space to greatly facilitate the release of hydrogen or oxygen. $(Ni_{1-x}Co_x)^{2+}Co_2{}^{3+}O_4$ has very similar crystalline structure with $NiCo_2O_4$ and Co_3O_4, possessing spinel *Fd3m* geometries.[22] Therefore, in the framework of N–$Ni_{1-x}Co_{2+x}O_4$ NPs in Fig. 1c, the vertex-sharing CoO_x or NiO_x polyhedrons are cross-linked by the O atom to build a three-dimensional framework. Some Co^{2+} and a few of O^{2-} are replaced by Ni^{2+} and N^{3-}, respectively. Atoms with different valences are shown by different colors (Fig. 1d). The X-ray diffraction (XRD) pattern of the as-grown N–$Ni_{1-x}Co_{2+x}O_4$ NPs is in good agreement with the DFT simulated pattern (Fig. 1e), justifying our theoretical crystal model. It should be noted that the (440) diffraction peak measured in the experiment is relatively wide, due to a slight deviation between the actual (440) peaks of $NiCo_2O_4$ and Co_3O_4.[23,24]

A close-up side-view of the nano-petals in Fig. 2a shows a thickness about 16 nm. The original SEM image is exhibited in ESI† Part 1 (ESI, P1). It is a layered structure by the superposition of several ultra-thin nano-layers (Fig. 2b). Fig. 2c is a typical transmission electron microscope (TEM) image of an ultra-thin N–$Ni_{1-x}Co_{2+x}O_4$ NP, which is obtained by ultrasonic peeling off from the nano-petals in DI water. Taken from the two red square regions in Fig. 2c and d demonstrates that the thickness of the ultra-thin NP is about 1–3 nm. The different lattice fringe images are shown in Fig. 2e by zooming in the blue region in Fig. 2c. Fig. 2f–h reveal the highly crystalline nature of the N–$Ni_{1-x}Co_{2+x}O_4$ NP with lattice spacings of 0.243, 0.285, and 0.233 nm, corresponding to the (311), (220) and (222) planes, respectively.[25,26] The spatial elemental analysis using electron energy loss spectroscopy (EELS) in Fig. 2i–l confirms that Co, Ni, O and N are distributed homogeneously throughout the selected flakes.

XPS analysis was carried out to further investigate the chemical states of the N–$Ni_{1-x}Co_{2+x}O_4$ NPs. Fig. 3a shows that the Ni 2p spectra consist of two groups of sub-peaks due to the spin–orbit coupling of the $2p_{1/2}$ and $2p_{3/2}$ states. For each group, there are three sub-peaks corresponding to Ni^{3+} and Ni^{2+} states, as well as a satellite peak. Similar to the Ni 2p, Fig. 3b reveals that the Co 2p spectra also include two sub-peaks due to the spin–orbit coupling of the $2p_{1/2}$ and $2p_{3/2}$ states.[27] The N 1s spectrum only contains the N^{3-}-metal chemical bond located at 398.2 eV (Fig. 3c), confirming that the N atoms only replace some of the O atoms.[28] In Fig. 3d, the O 1s spectrum of the as-grown sample without annealing consists of two sub-peaks due to the O^{2-}-metal and –OH chemical bonds. With the annealing time increasing from 0.5 to 1 h, the sub-peak corresponding to –OH gradually fade away, while the peak position of O^{2-}-metal bonds has a slight left-shift. This can be ascribed to that metal hydroxide is dehydrated and changed to oxide gradually during annealing, and nitrogen doping is produced during the thermal treatment.

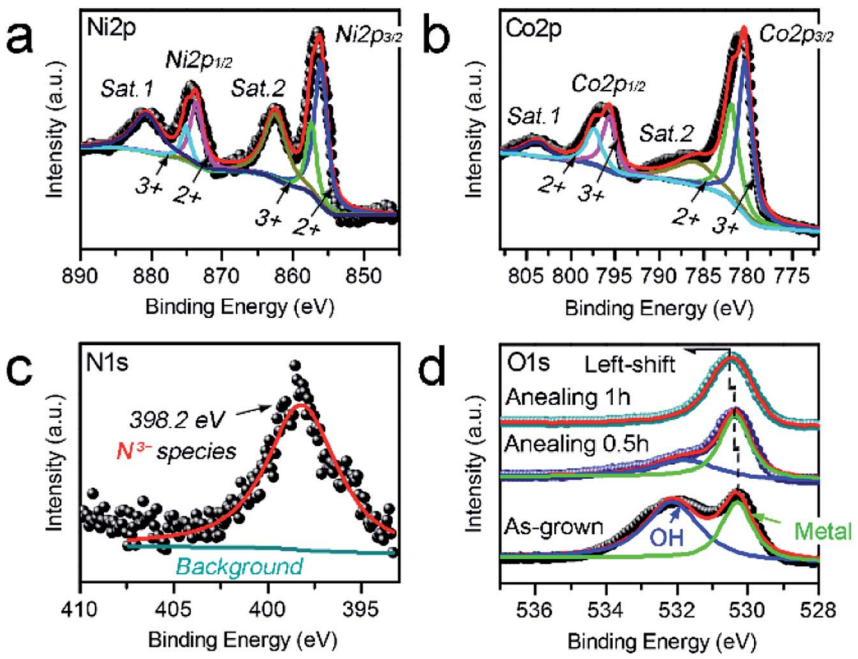

Fig. 3 (a–d) Ni 2p (a), Co 2p (b), N 1s (c) and O 1 s (d) XPS spectra measured from the N–$Ni_{1-x}Co_{2+x}O_4$ NPs.

3.2. Influences of CTAB and urea over the morphology and N-doping of samples

During the fabrication process, the concentrations of CTAB and urea demonstrate significant influences over the morphology and N-doping of samples, respectively. It was confirmed by SEM observation (ESI, P2†) that, without adding CTAB, the morphology of product was one-dimensional nanowire; as the CTAB concentration increased to 5 mmol L^{-1}, the product was a mixture composed by nanowires and nano-petals; with the CTAB concentration exceeded 10 mmol L^{-1}, the product was formed by pure nano-petals. Therefore, during the sample construction process of this work, CTAB, as a surfactant, inhibits the growth of the nanostructure along the *c*-axis into a one-dimensional acicular structure, and promotes the formation of two-dimensional sheet structure of the N–$Ni_{1-x}Co_{2+x}O_4$ NPs.

Besides, with the aid of XPS, we found that the concentration of doped nitrogen (at%) could be increased with urea (ESI, P3†). As the concentration of urea in hydrothermal-solution increasing from 0 to 1.0, 2.0 and 3.0 mmol L^{-1}, the N-doing concentration in samples increased from 1.36 to 2.20, 4.51 and 4.49%, respectively. Here, the N-doping of 1.36% may be induced by CTAB. This indicates that after the concentration of urea exceeds 3 mmol, the concentration of N-doping will not continue to increase.

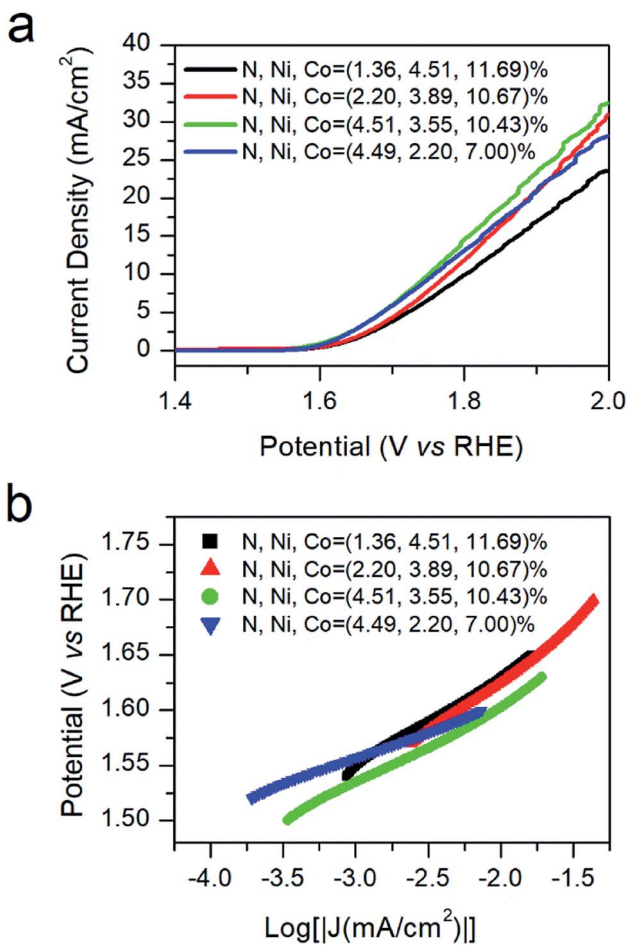

Fig. 4 OER LSV curves (a) and corresponding Tafel plots (b) of the N–$Ni_{1-x}Co_{2+x}O_4$ NPs with different N-doping concentrations.

3.3. Catalytic properties of Ni, Co-samples

3.3.1. OER measurements on Ni, Co-samples with different N-doping concentrations. The electrochemical water-splitting performance of the as-synthesized N–$Ni_{1-x}Co_{2+x}O_4$ NPs was measured by using a three-electrode system in 1.0 M KOH solution. *iR* correction was performed before measurements. Considering that, the OER has more complex electrochemical processes and higher kinetic barriers than those of HER. Therefore, we tested OER efficiency of samples with different N-doping concentrations. Fig. 4a confirms that the sample with N-doping concentration of 1.36% has the highest OER potential about 1.81 V *vs.* RHE at the current density of 10 mA cm^{-2}. As the N-doping concentration increases to 4.51%, the OER potential has the lowest value about 1.75 V *vs.* RHE. However, when the concentration of added urea is 3 mmol, the N-doping concentration is 4.49% and Ni, Co concentrations decrease to 2.20 and 7.00%, respectively (ESI, P3†). The OER potential degenerates to 1.76 V *vs.* RHE at the current density of 10 mA cm^{-2}. Thus, OER efficiency first increases and then decreases with the concentration of N-doping.

Derived from the logarithmic region of LSV curves in Fig. 4a, the Tafel slopes are employed to evaluate the HER kinetics difference of the four samples.[29] Fig. 4b demonstrates that the sample with the N-doping concentration of 4.51% has the lowest Tafel slope than those of others, showing the most efficient OER kinetics of all.

3.3.2. HER and OER measurements on Ni, Co-samples with different annealing conditions. Fig. 5a shows the HER linear sweeping voltammetry (LSV) curves of the as-synthesized samples without annealing, and annealed for 0.5, 1 and 1.5 h. The LSV curve of Pt/C was also given for comparison. The HER efficiencies of the samples first experience obvious improvement and then decrease with increasing the annealing time. At a current density of 10 mA cm^{-2}, the N–$Ni_{1-x}Co_{2+x}O_4$ NPs with 1 h annealing exhibits the lowest over-potential of 67.8 mV, which is quite close to the benchmark Pt/C electrode.

After HER analysis, the LSV curves for OER of all samples were measured (Fig. 5b). As expected, the sample with the annealing time of 1 h still has the lowest OER potential about 1.65 V *vs.* RHE at the current density of 10 mA cm^{-2}. As revealed by Fig. 5a and b, the samples with different annealing times exhibit different HER and OER efficiencies. It is essential to explore the mechanism for the effect of catalytic enhancement by annealing. Taken HER efficiency as an example, the Tafel slopes and active surface areas of the above four samples are compared and shown in Fig. 5c–f. Fig. 5c confirms that the sample with the annealing time of 1 h has the lowest Tafel slope, demonstrating the most efficient HER kinetics. And then, the double layer capacitances (C_{dl}) of the four samples are tested to compare the active surface areas. C_{dl} is derived from the slope obtained by fitting the plot of Δj as a function of the scanning rate of potential (mV s^{-1}). Fig. 5d and e collect the

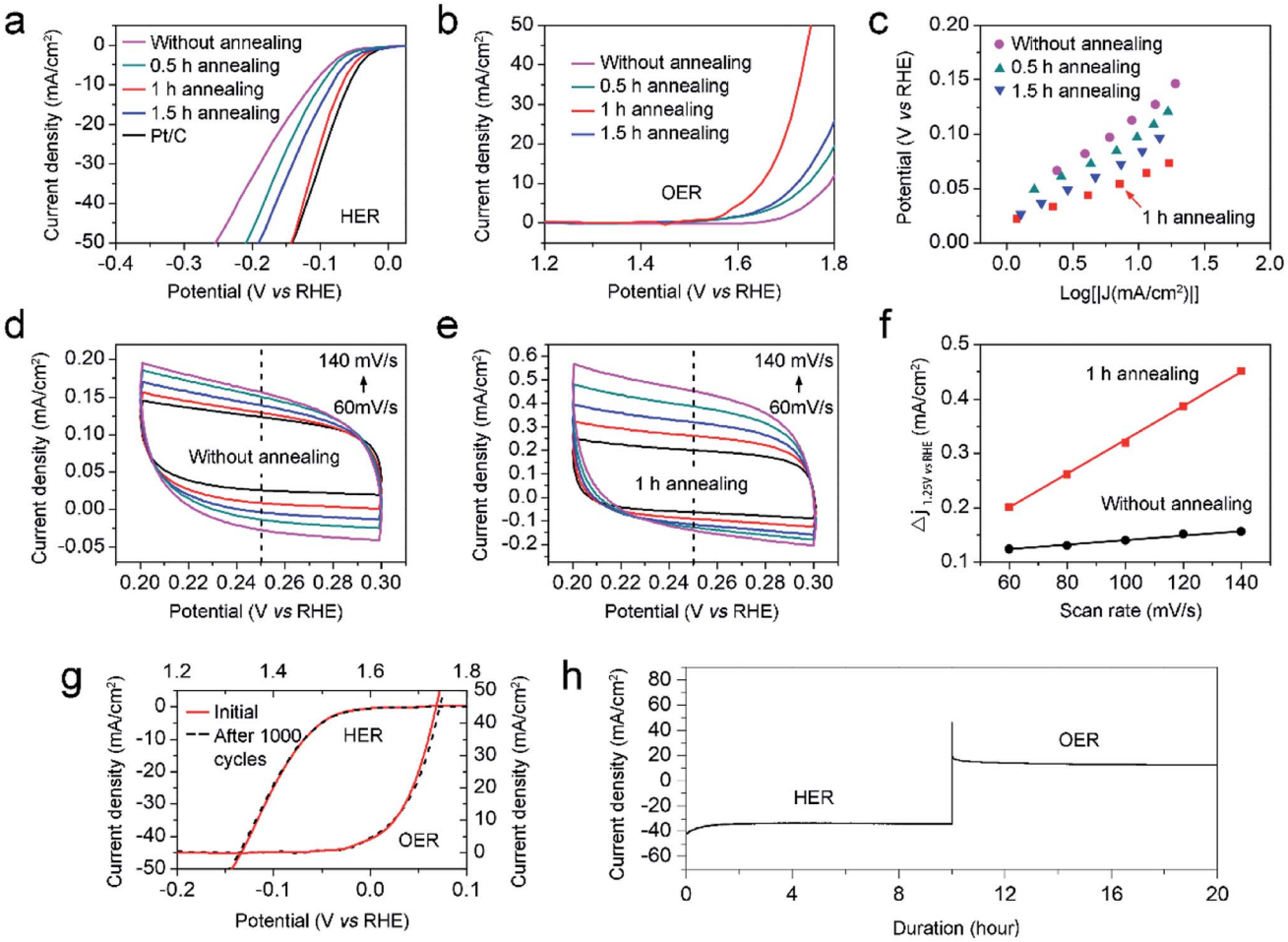

Fig. 5 (a and b) HER (a) and OER (b) LSV curves of the N–$Ni_{1-x}Co_{2+x}O_4$ NPs without annealing and annealed for 0.5, 1 and 1.5 h; (c) corresponding Tafel plots obtained from HER LSV curves; (d and e) CV curves of the N–$Ni_{1-x}Co_{2+x}O_4$ NPs without annealing (d) and annealed for 1 h (e) measured in a potential range of 0.2–0.3 V *vs.* RHE under the scan rates from 60 to 140 mV s^{-1}; (f) charging current density differences at 0.25 V *vs.* RHE ($\Delta j = j_a - j_c$) as a function of the scan rates; (g) HER and OER LSV curves of the N–$Ni_{1-x}Co_{2+x}O_4$ NPs before and after 1000 cycles; (h) HER and OER stability measurements of the N–$Ni_{1-x}Co_{2+x}O_4$ NPs.

closed CV curves in the region of 0.2 to 0.3 V *vs.* RHE for the samples without annealing and annealed for 1 h, respectively. Taking the RHE potential of 0.25 V as reference, the C_{dl} slope of the sample without annealing is lower than that annealed for 1 h, indicating that the electrochemical effective area can be increased by annealing. The above results reveal that the superior HER and OER efficiencies of the N–$Ni_{1-x}Co_{2+x}O_4$ NPs annealed for 1 h in alkaline media originates from the improved catalytic kinetics and increased active surface area.

3.3.3. HER and OER catalytic stability. In addition to electrocatalytic efficiency, electrode stability in alkaline environment is also very important. Fig. 5g demonstrates that the LSV curves of the N–$Ni_{1-x}Co_{2+x}O_4$ NPs with 1 h of annealing for both HER and OER almost experience no change even after 1000 cycles, revealing its ultra-reliable stability for HER and OER in alkaline conditions. The time-dependent current stabilities at fixed potentials in Fig. 5h also confirms that the HER and OER performances of the 1 h annealed N–$Ni_{1-x}Co_{2+x}O_4$ NPs maintain stable at least for 20 h (Fig. 5h).

3.3.4. Density functional theory calculation and discussion. All the above electrochemical experimental analyses show that appropriate annealing can significantly facilitate the electrocatalytic kinetics of the synthesized samples, for both HER and OER, we envision that nitrogen doping is the core reason for improving the HER and OER efficiencies of samples. Undoubtedly, numerous studies have shown that doping could produce oxygen vacancies and surface defects, which will greatly improve the catalytic performance of the samples. However, beyond increasing the number of oxygen vacancies and surface defects, we are still looking forward to exploring other significant contributions of nitrogen doping endowed to HER and OER. To realize this, density functional theory (DFT) calculation has been performed to check the changes of the internal crystalline characteristics of N–$Ni_{1-x}Co_{2+x}O_4$ NPs after nitrogen doping. The crystalline modeling is exhibited in Fig. S5a of ESI P4.† It can be clearly observed that the bond lengths between atoms and the densities of electron cloud varies obviously after nitrogen doping (Fig. S5b†). Fig. 6a and

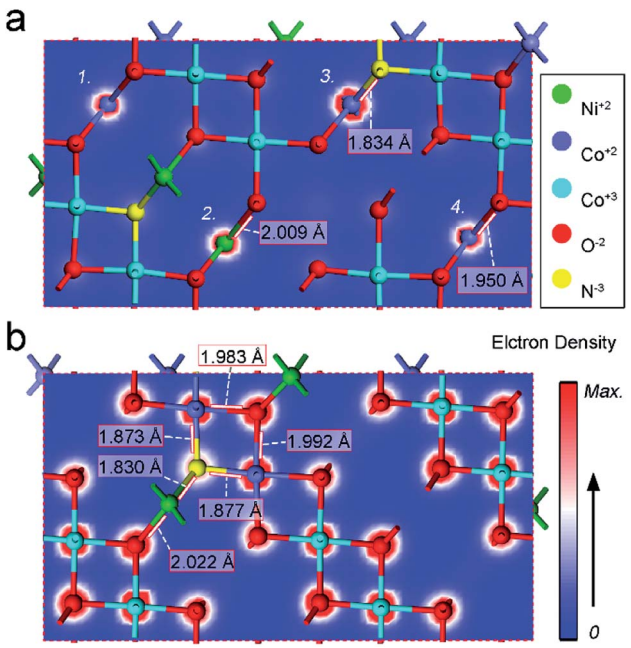

Fig. 6 (a and b) Electron densities in different cross sections in N–$Ni_{1-x}Co_{2+x}O_4$ NPs from DFT calculation.

b shows the top- and bottom-views of crystal structure with the electron density of the N–$Ni_{1-x}Co_{2+x}O_4$ NPs in specified cross sections. In Fig. 6a, only four atoms locate their centers in this cross section plane: one Ni^{2+} and three Co^{2+} atoms. It reveals that, if it only bonds with O^{2-} atoms, Ni^{2+} in location 2 has almost the same electron density with Co^{2+} in location 1 and 4; while if it is bonded with N^{3-} atoms, Co^{2+} possesses obviously enhanced electron density. Moreover, the length of the N–Co bond is shorter than O–Co and O–Ni bonds, indicating nitrogen doping can induce lattice contraction. From Fig. 6b we can see that the electron density of N^{3-} atoms is almost the same as that of O^{2-} atoms in the same periodic position, and the bond lengths between N^{3-} atom and the surrounding atoms are 1.830, 1.873 and 1.877 Å, respectively. It confirms that nitrogen doping does not increase the electron density of the N^{3-} atom itself, but shortens the bond length between the N^{3-} atom and the neighboring metal atoms. Therefore, we conclude that nitrogen doping not only creates oxygen vacancy or other defects in the crystal, but also significantly increases the electron density of the metal atoms attached to N^{3-} atoms, and furthermore shortens the atomic spacing of N-metal. The shortening of lattice spacing is an important factor for the enhancement of the HER and OER performances of electrocatalytic materials.

4. Conclusion

Large-area N–$Ni_{1-x}Co_{2+x}O_4$ nano-petals have been *in situ* synthesized on the surface of Ni foam by hydrothermal and annealing strategies. The annealing introduced N^{3-} atoms doping originates from the amino group in urea. The electrochemical measurements demonstrate that the N–$Ni_{1-x}Co_{2+x}O_4$ NPs with 1 h annealing have a low overpotential and a creditable stability for both HER and OER. DFT calculation reveals that, compared with bimetallic and bivalent mixing, nitrogen doping contributes more significantly to the improvement of HER and OER performances, which can be ascribed to the N-doped induced creation of defects such as oxygen vacancies, increase of the electron density of the metal atoms connected to N^{3-} atoms and the shortening of the bond length between N^{3-} and metal atoms. The successful synthesis of high-performance bi-functional N–$Ni_{1-x}Co_{2+x}O_4$ NPs opens a new avenue for rational design of effective electrocatalytic nanomaterials.

Conflicts of interest

There are no conflicts to declare.

Acknowledgements

This work was supported by the National Natural Science Foundation of China (No.51874029).

References

1 N. Cheng, S. Stambula, D. Wang, M. N. Banis, J. Liu, A. Riese, B. Xiao, R. Li, T. K. Sham, L. M. Li, G. A. Botton and X. Sun, *Nat. Commun.*, 2016, **7**, 13638.
2 C. Xu, P. K. Shen and Y. Liu, *J. Power Sources*, 2007, **164**, 527–531.
3 K. S. Exner, J. Anton, T. Jacob and H. Over, *ChemElectroChem*, 2015, **2**, 707–713.
4 Y. Lee, J. Suntivich, K. J. May, E. E. Perry and S. H. Yang, *J. Phys. Chem. Lett.*, 2012, **3**, 399–404.
5 C. Hitz and A. Lasia, *J. Electroanal. Chem.*, 2001, **500**, 213–222.
6 T. Zhang, M. Y. Wu, D. Y. Yan, J. Mao, H. Liu, W. B. Hu, X. W. Du, T. Ling and S. Z. Qiao, *Nano Energy*, 2018, **43**, 103–109.
7 X. Zhang, R. Liu, Y. Zang, G. Liu, G. Wang, Y. Zhang, H. Zhang and H. Zhao, *Chem. Commun.*, 2016, **52**, 5949.
8 Y. Zhao, B. Sun, X. Huang, H. Liu, D. Su, K. Sun and G. Wang, *J. Mater. Chem. A*, 2015, **3**, 5402–5408.
9 K. L. Nardi, N. Yang, C. F. Dickens, A. L. Strickler and S. F. Bent, *Adv. Energy Mater.*, 2015, **5**, 1500412.
10 J. W. D. Ng, M. García-Melchor, M. Bajdich, P. Chakthranont, C. Kirk, A. Vojvodicv and T. F. Jaramill, *Nat. Energy*, 2016, **1**, 16053.
11 X. Yan, K. X. Li, L. Lyu, F. Song, J. He, D. Niu, L. Liu, X. Hu and X. Chen, *ACS Appl. Mater. Interfaces*, 2016, **8**, 3208–3214.
12 N. Srinivasa, L. Shreenivasa, P. S. Adarakatti, J. R. N. Samuel, C. E. Banks and S. Ashoka, *RSC Adv.*, 2019, **9**, 24995–25002.
13 J. Zhao, Y. He, Z. Chen, X. Zheng, X. Han, D. Rao, C. Zhong, W. Hu and Y. Deng, *ACS Appl. Mater. Interfaces*, 2018, **11**, 4915–4921.
14 Y. Fu, H. Y. Yu, C. Jiang, T. H. Zhang, R. Zhan, X. Li, J. F. Li, J. H. Tian and R. Yang, *Adv. Funct. Mater.*, 2018, **28**, 1705094.
15 J. Diao, Y. Qiu, S. Liu, W. Wang, K. Chen, H. Li, W. Yuan, Y. Qu and X. Guo, *Adv. Mater.*, 2019, **32**, 1905679.

16 R. Zou, M. Xu, S. A. He, X. Han, R. Lin, Z. Cui, G. He, D. J. L. Brett, Z. Guo, J. Hu and I. P. Parkin, *J. Mater. Chem. A*, 2018, **6**, 19853–19862.
17 B. Chang, J. Yang, Y. Shao, L. Zhang, W. Fan, B. Huang, Y. Wu and X. Hao, *ChemSusChem*, 2018, **11**, 3198–3207.
18 L. Liu, F. Yan, K. Li, C. Zhu, Y. Xie, X. Zhang and Y. Chen, *J. Mater. Chem. A*, 2019, **7**, 1083–1091.
19 X. Peng, C. Pi, X. Zhang, S. Li, K. Huo and P. K. Chu, *Sustainable Energy Fuels*, 2019, **3**, 366–381.
20 X. Zou and Y. Zhang, *Chem. Soc. Rev.*, 2015, **44**, 5148–5180.
21 D. Kim, J. Park, J. Lee, Z. Zhang and K. Yong, *ChemSusChem*, 2018, **11**, 3618–3624.
22 L. Huang, D. Chen, Y. Ding, S. Feng, Z. L. Wang and M. Liu, *Nano Lett.*, 2013, **13**, 3135–3139.
23 F. Deng, L. Yu, G. Cheng, T. Lin, M. Sun, F. Ye and Y. Li, *J. Power Sources*, 2014, **251**, 202–207.
24 P. Vikas, J. Pradeep, C. Manik and S. Shashwati, *Soft Nanosci. Lett.*, 2012, **2**, 1–7.
25 J. Béjar, L. Álvarez-Contreras, J. Ledesma-García, N. Arjona and L. G. Arriagaa, *J. Electroanal. Chem.*, 2019, **847**, 113190.
26 H. Xu, Z. X. Shi, Y. X. Tong and G. R. Li, *Adv. Mater.*, 2018, **30**, 1705442.
27 Y. Guo, P. Yuan, J. Zhang, H. Xia, F. Cheng, M. Zhou, J. Li, Y. Qiao, S. Mu and Q. Xu, *Adv. Funct. Mater.*, 2018, **28**, 1805641.
28 M. Yu, Z. Wang, C. Hou, Z. Wang, C. Liang, C. Zhao, Y. Tong, X. Lu and S. Yang, *Adv. Mater.*, 2017, **29**, 1602868.
29 B. Chen, Z. Zhang, S. Kim, S. Lee, J. Lee, W. Kim and K. Yong, *ACS Appl. Mater. Interfaces*, 2018, **10**, 44518–44526.